Study of the Electromagnetic Properties of Nano $(M_xZn_{1-x})Fe_2O_4$ (M=Cu, Ni) as a Function of the Sintering Temperature

Yenchun Liu * and Jarnchih Hsu

Graduate School of OptoMechatronics and Materials, WuFeng University, Chiayi 62153, Taiwan; billy88094266@gmail.com

* Correspondence: blliu@wfu.edu.tw; Tel.: +886-953-303-683; Fax: +886-5-206-3264

check for updates

Featured Application: The obtained results suggest that the prepared $(M_xZn_{1-x})Fe_2O_4$ (M=Cu, Ni) ferrite nanoparticles are a promising as catalysts or iron core applications.

Abstract: In this study, the chemical co-precipitation method was used to prepare a nanoscale ferrite powder with Cu-Zn and Ni-Zn compositions. Ferrite, in different Cu-Zn stoichiometric ratios, showed optimal composition of saturated magnetization for $Cu_{0.7}Zn_{0.3}Fe_2O_4$; under an air environment and calcined at 900 °C, the saturated magnetization was 60.19 M(emu/g). The average particle diameter was 10 nm for the non-calcined sample, while when the sintering temperature was 900 °C, the particle diameter was about 150 nm. In addition, in different Ni-Zn stoichiometric ratios, the optimal composition of the saturated magnetization was $Ni_{0.5}Zn_{0.5}Fe_2O_4$; under an air environment and calcination at 900 °C, the saturated magnetization was 91.40 M(emu/g). The average particle diameter for the non-calcined sample was about 10 nm, but when the sintering temperature was 1200 °C, the particle diameter was 201.06 nm. The prepared ferrite nano-powder was characterized by scanning electron microscopy(SEM), X-ray diffraction(XRD), and vibrating sample magnetometer(VSM) to reveal its microscopic structure and related electromagnetic properties. Ferrite powders of either Cu-Zn or Ni-Zn composition can be used as catalysts for chemical reactions or iron core materials.

Keywords: co-precipitation method; ferrite; saturated magnetization

1. Introduction

The origin of ferrite dates from very early in time, and it usually existed as Fe_3O_4, as natural ferrite. Ferrite is an oxide of strong magnetic properties, with wide applications due to the booming development of electronic technology. Nowadays, it has become an indispensable material in the electronics industry. The production of ferrite was originally made through the calcination of an inorganic precursor material; therefore, its process was the same as that of ceramics and it belonged to the products of the ceramics industry. In its production, highly pure precursor materials were used, and the sintering environment and condition were controlled, as such, it is considered the earliest fine ceramic in history [1,2]. Based on the structure, ferrite can be divided into three main categories [3]: spinel structure, garnet structure, and hexagonal structure. Methods for the preparation of ferrite can be roughly divided into: solid-state reaction [4–6], co-precipitation [7–9], sol-gel [10–12], and hydrothermal processes [13–15]. The ferrites in nanocrystalline form found applications in new fields, such as magnetically guided drug delivery, magnetic resonance imaging (MRI), catalysts, humidity and gas sensors, magnetic fluids, etc. [16,17]. Presently, ferrite core has become an

indispensable inductive component in 3C products. In this work, the pure material and the co-precipitation method were used to prepare Cu-Zn and Ni-Zn ferrite nano-powders and investigate their magnetic characteristics, particle diameters, and magnetic flux densities, etc. The co-precipitation method was used at different pH values (from 6 to 12) and different sintering temperatures (from 0 °C to 1200 °C) to synthesize $[Cu_xZn_{1-x}]Fe_2O_4$, $[Ni_xZn_{1-x}]Fe_2O_4$ ferrite powders. Then, the effect of the pH value on crystallinity and integrity was investigated, and the effect of sintering temperature on saturated magnetization (Ms), residual magnetization (Mr), coercive force (Hc), magnetic flux (B), and average particle diameter (D) was also studied.

In 2008, Ewaisn used the solid-state reaction method to prepare $ZnO-MnO_2-Fe_2O_3$; as the sintering temperature increased, the saturated magnetization also increased. Moreover, as the sintering temperature increased to 1150 °C, a maximum was reached, followed by a decline. When the temperature reached 1050 °C–1100 °C, the surface morphology was transformed from the original cluster into a chain shape, and when the sintering temperature reached 1150 °C–1200 °C, it was transformed into a laminating structure [4]. For the preparation of Ni-Cu-Zn ferrite nanoparticles using the chemical co-precipitation method and for the study of magnetic property after sintering, high purity Ni_2SO_4, $CuSO_4$, $ZnSO_4$, and ferrous sulfate were used as precursor materials dissolved in water, with NaOH being used as the precipitation agent to form $Ni_{0.39}Cu_{0.11}Zn_{0.5}Fe_2O_4$ with an obtained average particle diameter of about 30 nm. When Cu is added to ferrite, the density and magnetization can be increased. In 2011, Song et al. used strontium nitrate, nickel acetate, zinc acetate, ferric nitrate, and citric acid as precursor materials, and employed the sol-gel process to prepare ferrite nanofibers and $SrFe_{12}O_{19}/Ni_{0.5}Zn_{0.5}Fe_2O_4$ nanocomposite ferrite. Single $Ni_{0.5}Zn_{0.5}Fe_2O_4$ ultra fine fiber ferrite showed a particulate structure with a shiny surface morphology. Single $SrFe_{12}O_{19}$ ultra-fine fiber ferrite showed a pillared structure [11]. An increase in the calcination temperature of the nanocomposite $SrFe_{12}O_{19}/Ni_{0.5}Zn_{0.5}Fe_2O_4$ ferrite caused a slow change from an original nanoparticle into a laminating structure. When the sintering temperature reached 1150 °C, a hexagonal laminating structure with a rough surface was observed. In 2008, Deliyanni et al. used ammonia as a precipitation agent and used aqueous metal precursors to prepare Mn-Zn ferrite, and an integrated spinel structure with high specific area was obtained. The average particulate diameter was in the range of 5–25 nm [18,19]. The average diameter was around 17 nm. Such a crystalline structure was very close to the results obtained by the Scherrer equation, that is, nanocrystals with a diameter of 13.5 nm, and such results were consistent with each other. Other authors, such as Murbe et al., prepared Ni-Cu-Zn ferrites of composition $Ni_{1-x-y}Cu_y Zn_x Fe_2O_4$ with $0.4 \lneq x \lneq 0.6$ and $0 \lneq y \lneq 0.25$ by standard ceramic processing routes and studied the effect on the sintering behavior and permeability [20].

2. Experimental

2.1. Materials and Measuring Tools

The sulfuric acid (H_2SO_4), hydrochloric acid (HCl), sodium hydroxide (NaOH), zinc(II) nitrate ($Zn(NO_3)_2 \cdot 6H_2O$), ferric(III) nitrate ($Fe(NO_3)_3 \cdot 9H_2O$), nickel nitrate, ($Ni(NO_3)_2 \cdot 6H_2O$), and other reagents were all G. R. grade chemicals for synthesis. A computer-interface X-ray powder diffractometer (XRD) with Cu Kα radiation (Multiflex, Rigaku, Tokyo, Japan) was used to identify the nanoparticles. Particle morphology was checked using a scanning electron microscope (SEM, Hitachi S3000N, Tokyo, Japan) with an accelerating voltage of 15 kV, and a field emission scanning electron microscope (FESEM, JEOL, JSM-6700F, Tokyo, Japan) was used to characterize the surface structure of the distribution of nanoparticles. A Vibrating Sample Magnetometer (VSM, ADE-DMS 1660, MA, USA) was used to observe the nanoparticles' electromagnetic properties. The oxygen analyzer measured the oxygen concentration (Chang-Ai, CI1000, Shanghai, China). The composite particles of ferrite were prepared by sintering in a high temperature furnace (AcuTech systems Co., Ltd. BAT-750, New Taipei, Taiwan).

2.2. Synthesis of $[M_xZn_{1-x}]Fe_2O_4$ (M=Cu or Ni)

Ionic solutions of $CuSO_4$, $Ni(NO_3)_2$, $Zn(NO_3)_2$, and $Fe(NO_3)_3$ were mixed according to the desired stoichiometric ratio. NaOH solution was used to adjust to pH = 9. Air was passed and the solution was heated up to 80 °C and left to oxidize for 24 h. Distilled water was used to repeatedly clean (5–6 times) the product to remove the salt. Then the product was placed in an oven at 120 °C for 1–2 days, depending on the water content, until total evaporation was achieved. Then it was grinded on an agate mortar. The chemical formula is shown in the flow chart of Figure 1.
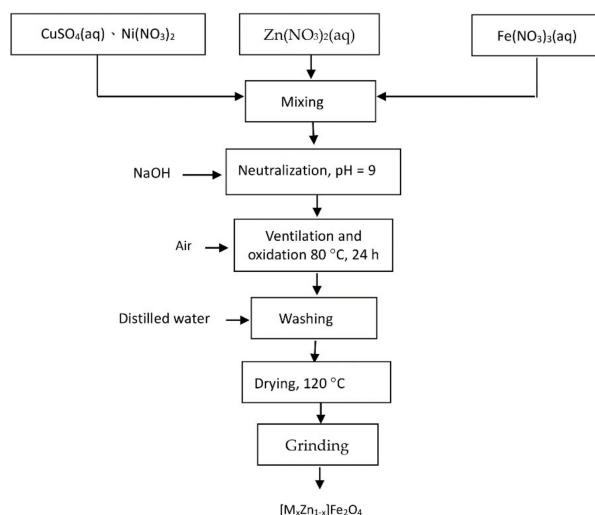

Figure 1. $[M_xZn_{1-x}]Fe_2O_4$ ferrite synthesis.

3. Results and Discussion

Ferrite can be divided into two main categories, namely, soft ferrite and hard ferrite, according to its applications. Soft ferrite is defined as having an Hc not larger than 200 Oe, when magnetization occurs; hence, the smallest externally applied magnetic field can be used to reach the maximal magnetization strength. The features of soft ferrite include a lower coercive force and higher magnetic permeability; that is, it can be easily magnetized and de-magnetized and is therefore is widely used for electronic materials. Hard ferrite is obtained after the material is magnetized by an externally applied magnetic field, and its magnetic properties are maintained in the long term. The features of hard ferrite include a higher coercive force (the magnetic field strength for the residual magnetization is reduced to zero after the magnetic material is magnetized and de-magnetized), higher residual magnetic flux density (Br), higher residual magnetization (Mr), higher stability (to environmental variation factors, such as externally applied magnetic field and vibration), and higher maximum energy product (Bh).

In this work, a co-precipitation method was used to prepare nanoscale ferrite, and a metal solution was added with NaOH as a precipitation agent. Then, air was passed to heat up and oxidize the product so that the hydroxide was changed into ferrite with a spinel structure. $[M_xZn_{1-x}]Fe_2O_4$ (M=Cu or Ni) was prepared at different conditions, and the effect on crystal phase, surface morphology, average particulate diameter, and magnetic properties was investigated.

3.1. The Influence of Different Cu and Ni Contents on the Crystal Phase of Ferrite

From the diffraction peaks of the XRD diffractograms of $[Cu_xZn_{1-x}]Fe_2O_4$ with different Cu contents and proportions, it can be seen that the change in the proportions also affects the crystal phase strength. $Cu_{0.7}Zn_{0.3}Fe_2O_4$ is the most integrated and the strongest crystal phase, while $Cu_1Fe_2O_4$ is the least integrated and the weakest one. Using the diffraction peaks and the Scherrer equation, the average particulate diameter was calculated. Based on the data, it can be seen that the particulate

diameter changed along with the strength of the crystal phase. For a composition of $Cu_{0.7}Zn_{0.3}Fe_2O_4$, with the strongest strength of crystal phase, the average particulate diameter was also the largest (22.32 nm). For the composition of $Cu_1Fe_2O_4$, the strength of the crystal phase was the weakest, and the average particulate diameter was the smallest (only 4.66 nm). Figure 2a shows the XRD diagram with different proportions of $[Cu_xZn_{1-x}]Fe_2O_4$ sintered at 600 °C. For different proportions, sintering at 600 °C (temperature increase of 5 °C/min, and kept at constant temperature for 2 h) was used to enhance the crystal phase and facilitate comparison. From the figure, it can be seen that when the Zn content was too low, Cu in $[Cu_xZn_{1-x}]Fe_2O_4$ could be easily transformed into CuO, and when the Zn content was zero, the strength of the crystal phase of CuO was stronger.
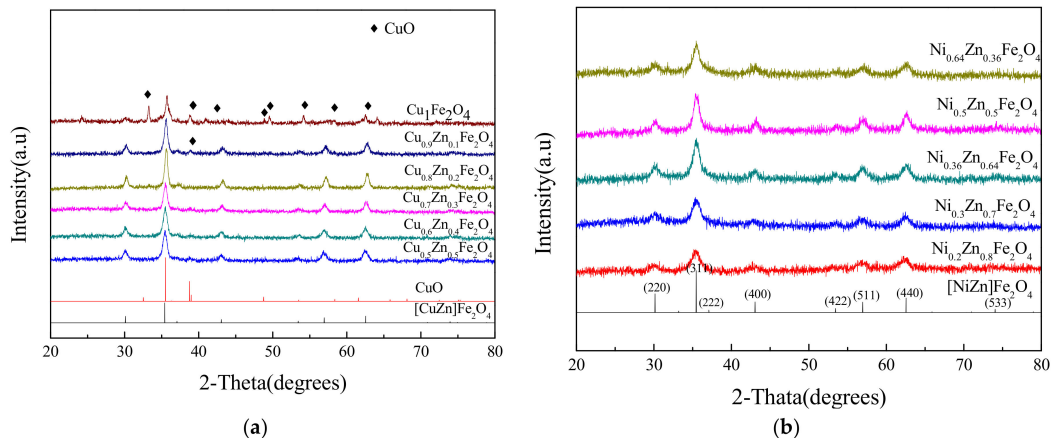
**Figure 2.** The X-ray powder diffraction (XRD) patterns of $[M_xZn_{1-x}]Fe_2O_4$ sintered at 600 °C. (**a**) $[Cu_xZn_{1-x}]Fe_2O_4$; (**b**) $[Ni_xZn_{1-x}]Fe_2O_4$.

Figure 2b shows $[Ni_xZn_{1-x}]Fe_2O_4$ ferrite. The proportion of Ni and Zn was changed to investigate the differences in the crystal phase. From the diffraction peaks, it can be seen that the change of the proportion also affects the strength of the crystal phase. The samples with strongest crystal phases were $Ni_{0.36}Zn_{0.64}Fe_2O_4$, $Ni_{0.5}Zn_{0.5}Fe_2O_4$, and $Ni_{0.64}Zn_{0.36}Fe_2O_4$ ferrite, the saturated magnetization of these three sets of proportions was relatively stronger. The diffraction peaks were then used to calculate the particulate diameter that was in the range of 10.92 nm to 19.6 nm. The average particulate diameter of $Ni_{0.5}Zn_{0.5}Fe_2O_4$ ferrite was the largest (about 19.60 nm). This was because $Ni_{0.5}Zn_{0.5}Fe_2O_4$ ferrite, as it can be seen from the XRD results, exhibited the most integrated and the strongest crystal phase. $Ni_{0.2}Zn_{0.8}Fe_2O_4$ ferrite had the smallest particulate diameter of 10.92 nm. It can be seen from the XRD results that the crystal phase strength of this composition and proportion was the weakest.

3.2. The Influence of Different Cu and Ni Contents on Magnetic Properties

Along with the change in the size and direction of the externally applied magnetic field, the magnetization state of the material started to deflect; after de-magnetization, the magnetic domain can return to its origin. The B, H slope caused by such a reversible boundary movement is called the initial permeability. When the magnetic field continues to increase and changes into an irreversible state, magnetization finally will reach saturation; at this moment, even if the externally applied magnetic field is enhanced, the magnetization strength cannot be increased. After magnetization reaches saturation, if the externally applied magnetic field is removed, some magnetic domains will remain the same with remanent magnetization (Br). If at this moment, a reverse magnetic field is added, then magnetization will, at coercive force (Hc), be reduced to zero. If the reversed externally applied magnetic field is continuously increased, the material will reach a saturated magnetization state that is the reverse of the original magnetization direction. When the externally applied magnetic field has cycled once from the positive direction to the negative direction, a hysteresis curve will be generated [21]. Figure 3a shows

the hysteresis curve for $[Cu_xZn_{1-x}]Fe_2O_4$ at different compositions and proportions. From the figure, it can be seen that saturated magnetization was 15.30 M(emu/g) for the composition and proportion of $Cu_{0.5}Zn_{0.5}Fe_2O_4$. As the Cu content increased, saturated magnetization also increased. When the Cu content reached $Cu_{0.7}Zn_{0.3}Fe_2O_4$, the saturated magnetization also reached a peak of 24.89 M(emu/g), and the crystal phase was the strongest too; later on, as the Cu content increased, the saturated magnetization decreased accordingly. When the Cu content reached the composition of $Cu_1Fe_2O_4$, the saturated magnetization was the lowest, only 1.20 M(emu/g), and its crystal phase was also the weakest.
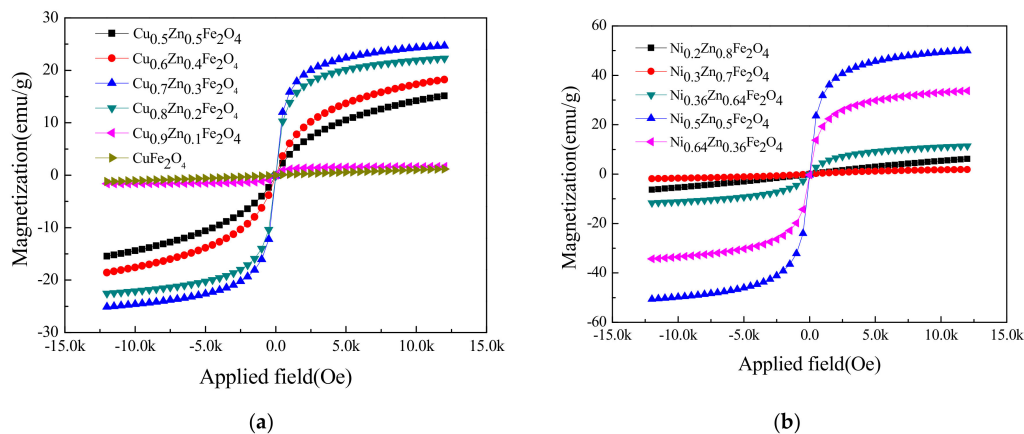
Figure 3. Hysteresis curves of $[M_xZn_{1-x}]Fe_2O_4$ at different compositions and proportions. (**a**) $[Cu_xZn_{1-x}]Fe_2O_4$; (**b**) $[Ni_xZn_{1-x}]Fe_2O_4$.

Concerning the Ni-Zn system, Figure 3b shows that $Ni_{0.5}Zn_{0.5}Fe_2O_4$ ferrite had the optimal magnetization, which was 50.29 M(emu/g), and its crystal phase was the strongest. $Ni_{0.3}Zn_{0.7}Fe_2O_4$ ferrite was the worst, at only about 1.86 M(emu/g), and its crystal phase was relatively weaker as well. Therefore, it is clear that the strength of the crystal phase can affect the magnetization of ferrite; however, the product with the worst crystal phase will not have the worst magnetization.

Table 1 depicts the coercive force (Hc), saturated magnetization (Ms), and residual magnetization (Mr) of $[Cu_xZn_{1-x}]Fe_2O_4$ at different proportions. From the data, it can be seen that the magnetic characteristic and Hc values for different proportions did not exceed 200 Oe, and the Mr value (soft ferrite had lower remanent magnetization) approached zero. Therefore, we can be sure that we are dealing with soft ferrite. For the magnetic flux of $[Cu_xZn_{1-x}]Fe_2O_4$ at different compositions and proportions, from the formula, the units of magnetic flux (B) are gauss, and the table shows that the magnetic flux for $Cu_{0.5}Zn_{0.5}$ was 186.12 gauss/g; as the Cu content increased, the magnetic flux increased accordingly. When the composition was $Cu_{0.7}Zn_{0.3}$, it reached a peak of 306.39 gauss/g; later on, it dropped, since for $Cu_1Fe_2O_4$, the magnetic flux was only 15.47 gauss/g. In terms of coercive force (Hc), saturated magnetization (Ms), and remanent magnetization (Mr) for $[Ni_xZn_{1-x}]Fe_2O_4$ ferrite with different proportions, the experimental results show that the magnetic characteristic and Hc values did not exceed 200 Oe, and the Mr value approached zero. Therefore, we can be sure that we are dealing with soft ferrite in this series. For the magnetic flux of $[Ni_xZn_{1-x}]Fe_2O_4$ ferrite, further calculations from the formula showed that the units of magnetic flux (B) were gauss. From the results, it can be seen that the magnetic flux for $Ni_{0.2}Zn_{0.8}$ was 61.18 gauss/g. For $Ni_{0.3}Zn_{0.7}$, the magnetic flux dropped to 14.00 gauss/g; later on, as Ni content increased, the magnetic flux also increased. When the composition was $Ni_{0.5}Zn_{0.5}$, it reached a peak of 624.48 gauss/g, but when the composition was $Ni_{0.64}Zn_{0.36}$, the magnetic flux decayed to 416.06 gauss/g. This trend was the same as the magnetic flux trend described in the literature [22,23]. The magnetic flux increases with the rise in Ni^{2+} ions concentration.

Table 1. The hysteresis curve for $[M_xZn_{1-x}]$ Fe_2O_4 at different compositions and proportions; Hc: Coercive force; Ms: Saturated magnetization; Mr: Residual magnetization; B: Magnetic flux.

Composition	Properties Magnetic	Hc (Oe)	Ms (emu/g)	Mr (emu/g)	B (gauss/g)
Cu-Zn system	$Cu_{0.5}Zn_{0.5}$	−6.05	15.30	−0.03	186.12
	$Cu_{0.6}Zn_{0.4}$	−12.48	18.41	−0.09	218.75
	$Cu_{0.7}Zn_{0.3}$	−6.23	24.89	−0.15	306.39
	$Cu_{0.8}Zn_{0.2}$	−5.87	22.42	−0.12	275.74
	$Cu_{0.9}Zn_{0.1}$	−4.25	1.62	−0.01	16.05
	$Cu_1Fe_2O_4$	0.35	1.20	0.00	15.47
Ni-Zn system	$Ni_{0.2}Zn_{0.8}$	−17.14	6.24	−0.01	61.18
	$Ni_{0.3}Zn_{0.7}$	−9.35	1.86	−0.00	14.00
	$Ni_{0.36}Zn_{0.64}$	−6.91	11.54	−0.04	108.04
	$Ni_{0.5}Zn_{0.5}$	−7.16	50.29	−0.34	624.48
	$Ni_{0.64}Zn_{0.36}$	−11.23	34.02	−0.32	416.06

3.3. The Effect of the Sintering Temperature on the Crystal Phase of $[Cu_xZn_{1-x}]Fe_2O_4$ and $[Ni_xZn_{1-x}]Fe_2O_4$

Figure 4a shows the XRD diagram of $Cu_{0.7}Zn_{0.3}Fe_2O_4$ at different sintering temperatures. The material was sintered in an air atmosphere, at 5 °C/min, and after a constant temperature maintained for 2 h the furnace was cooled. From the experimental results, it is clear that as the sintering temperature increased, the crystal phase became more integrated and its strength became stronger. Under the air sintering temperature and atmosphere, part of it suffered thermal decomposition due to over-heating; therefore, nitrogen was not needed in the sintering process. For the ferrite composition of $Cu_{0.7}Zn_{0.3}Fe_2O_4$, using the diffraction peaks at different sintering temperatures and the Scherrer equation, the average particulate diameter was calculated. And as temperature increased, the original particulate diameter of 24.65 nm at 500 °C increased to 94.46 nm at 900 °C. Thus, as the temperature increased, the particulate diameter also increased. Figure 4b shows the XRD diagram of $Ni_{0.5}Zn_{0.5}Fe_2O_4$ at different sintering temperatures, sintered in an air atmosphere at 5 °C/min, held at a constant temperature for 2 h, and finally furnace-cooled. The experimental results show that as the sintering temperature increased, the crystal phase became more integrated and its strength became stronger. This was unlike the $[Mn_xZn_{1-x}]Fe_2O_4$ system under air atmosphere, as when the sintering temperature was too high, thermal decomposition occurred. Therefore, N_2 was not needed for sintering. For $Ni_{0.5}Zn_{0.5}Fe_2O_4$ ferrite at different sintering temperatures, the diffraction peaks were used to calculate the average particulate diameters, and it was seen that the particulate diameter increased with the temperature increase. The particulate diameter increased from the original 20.31 nm at 500 °C to 201.06 nm at 1200 °C. The XRD diagram confirmed the single crystalline phase of the nanoparticles. The lattice parameter decreased with the increase in Ni content and reduced lattice strain.
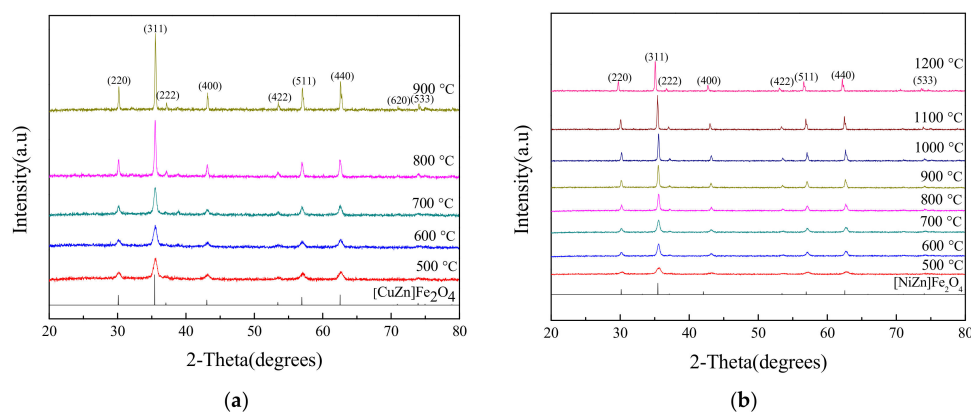
Figure 4. The effect of sintering temperature on the XRD pattern. (**a**) $Cu_{0.7}Zn_{0.3}Fe_2O_4$; (**b**) $Ni_{0.5}Zn_{0.5}Fe_2O_4$.

3.4. The Effect of Sintering Temperature on the Magnetism of $[Cu_xZn_{1-x}]$ Fe_2O_4, $[Ni_xZn_{1-x}]Fe_2O_4$ Ferrite

Figure 5a shows the hysteresis curve of $Cu_{0.7}Zn_{0.3}Fe_2O_4$ at different temperatures, sintered in an air atmosphere at 5 °C/min, held at a constant temperature for 2 h, and finally furnace-cooled. It can be seen that the worst saturated magnetization occurred at 500 °C, only 44.56 emu/g. However, as sintering temperature increased, the saturated magnetization also increased. When the sintering temperature reached 900 °C, the saturated magnetization reached a peak of 58.40 emu/g. For $Cu_{0.7}Zn_{0.3}Fe_2O_4$, the change of the saturated magnetization with the temperature was not as large as that observed for $[Mn_xZn_{1-x}]Fe_2O_4$ and $[Ni_xZn_{1-x}]Fe_2O_4$. Figure 5b shows the hysteresis curve for $Ni_{0.5}Zn_{0.5}Fe_2O_4$ ferrite at different sintering temperatures. It can be seen that the saturated magnetization was worse at 500 °C: 63.70 M(emu/g). As the sintering temperature increased, the saturated magnetization also increased, and when the sintering temperature reached 900 °C, the saturated magnetization reached a peak of 91.40 M(emu/g). Above 900 °C, the saturated magnetization started to decay, and when the sintering temperature reached 1200 °C, the saturated magnetization was only 69.92 M(emu/g).
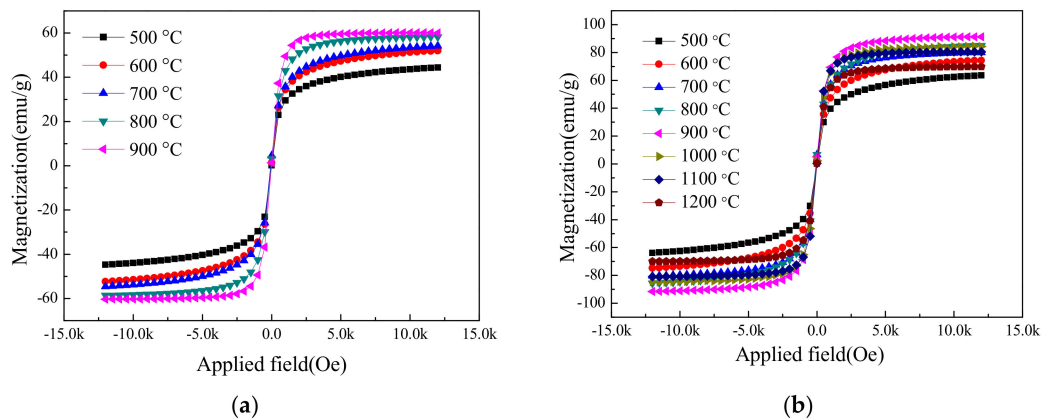
**Figure 5.** The effect of sintering temperature on the magnetism. (**a**) $Cu_{0.7}Zn_{0.3}Fe_2O_4$; (**b**) $Ni_{0.5}Zn_{0.5}Fe_2O_4$.

Table 2 shows the coercive force (Hc), saturated magnetization(Ms), and remanent magnetization (Mr) at different sintering temperatures for $[Cu_xZn_{1-x}]Fe_2O_4$. For $Cu_{0.7}Zn_{0.3}Fe_2O_4$, it can be seen that at different temperatures, the magnetic characteristic and Hc value did not exceed 200 Oe and the Mr value approached zero (soft ferrite had lower remanent magnetization). Therefore, we can be sure that this series of ferrite was composed of soft ferrites. For the magnetic flux of $[Cu_xZn_{1-x}]Fe_2O_4$ at different sintering temperatures, further calculations showed that the magnetic flux (B) increased from 562.99 gauss/g at 500 °C to 773.41 gauss/g at 700 °C as the temperature increased. Moreover, a peak of 781.28 gauss/g was seen at 800 °C, while at 900 °C, due to the smaller Hc value, the magnetic flux showed a small drop to 773.41 gauss/g. For $Ni_{0.5}Zn_{0.5}Fe_2O_4$ ferrite, the magnetic properties at different temperatures could be obtained, the Hc values did not exceed 200 Oe, and the Mr values approached zero (soft ferrite had lower remanent magnetization). Therefore, this series was also confirmed to be composed of soft ferrites. Moreover, magnetic fluxes (B) at different sintering temperatures increased from 801.62 gauss/g at 500 °C along with the temperature increase. When the temperature reached 900 °C, it reached a peak of 1193.72 gauss/g; later on, it started to drop, and when the temperature reached 1200 °C, the magnetic flux was only 886.31 gauss/g.

**Table 2.** The effect of sintering temperature on the magnetism of ferrite.

Composition/Temperature, °C	Properties Magnetic	Hc (Oe)	Ms (emu/g)	Mr (emu/g)	B (gauss/g)
$Cu_{0.7}Zn_{0.3}Fe_2O_4$	500	3.32	44.56	0.16	562.99
	600	23.92	52.24	1.33	680.05
	700	75.69	54.39	4.58	758.83
	800	47.78	58.40	3.16	781.28
	900	17.42	60.19	1.33	773.41
$Ni_{0.5}Zn_{0.5}Fe_2O_4$	500	1.55	63.70	0.09	801.62
	600	31.98	74.60	2.43	968.96
	700	71.79	80.20	6.70	1079.1
	800	69.54	85.28	6.64	1140.91
	900	45.74	91.40	5.08	1193.72
	1000	22.29	84.68	2.17	1085.87
	1100	4.06	80.72	0.43	1017.9
	1200	8.11	69.92	0.67	886.31

3.5. Surface Morphology Analysis of [CuZn]Fe₂O₄

Figure 6 shows the surface morphologies of $Cu_{0.7}Zn_{0.3}Fe_2O_4$ at different sintering temperatures, in an air atmosphere at 5 °C/min, held at a constant temperature for 2 h, and lastly cooled. It can be seen that the non-sintered powder had very small particulate diameter, and the average particulate diameter was about 10 nm. When sintering temperature increased to 500 °C, the SEM image showed that there was no significant difference, and the average particulate diameter was still about 20 nm. When sintering temperature was 600 °C, there was also no significant difference, as the average particulate diameter was still about 25 nm. At 700 °C, it can be seen that the primary particle started to grow significantly larger, and the average particulate diameter approached 50 nm. When the sintering temperature was 800 °C, the primary particles started to crystallize to form secondary particles, and the average diameter approached 70 nm. At 900 °C, the phenomenon of crystallization into secondary particles was more significant than that observed at 800 °C, and the average particulate diameter reached about 150 nm. In the observation of non-sintered $Cu_{0.7}Zn_{0.3}Fe_2O_4$ micro-structure, since the non-sintered powder has a very fine average particulate diameter, even on the SEM images with a 50,000× amplification the average particulate diameter could not be seen. From the 100,000× SEM image, it can be clearly seen that the average particulate diameter was about 10 nm. The electronic data systems(EDS) composition analysis showed that ferrite powder was an alloy formed by four elements; Mn, Zn, Fe, and O, and that no other metal atoms were present. Meanwhile, the proportion was correct, proving that, when neutralized, the metal ions were completely precipitated.

(a)   (b)

Figure 6. *Cont.*

(c)

(d)

(e)

(f)
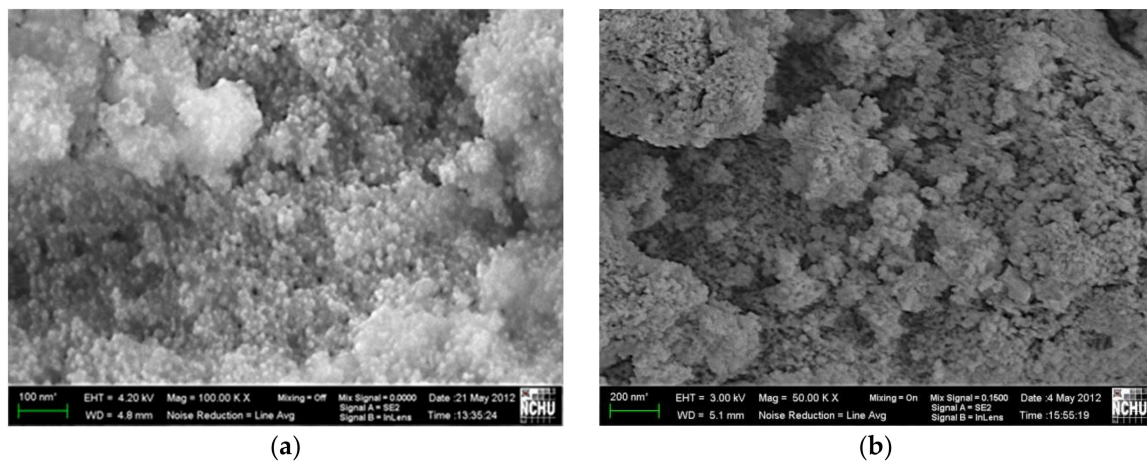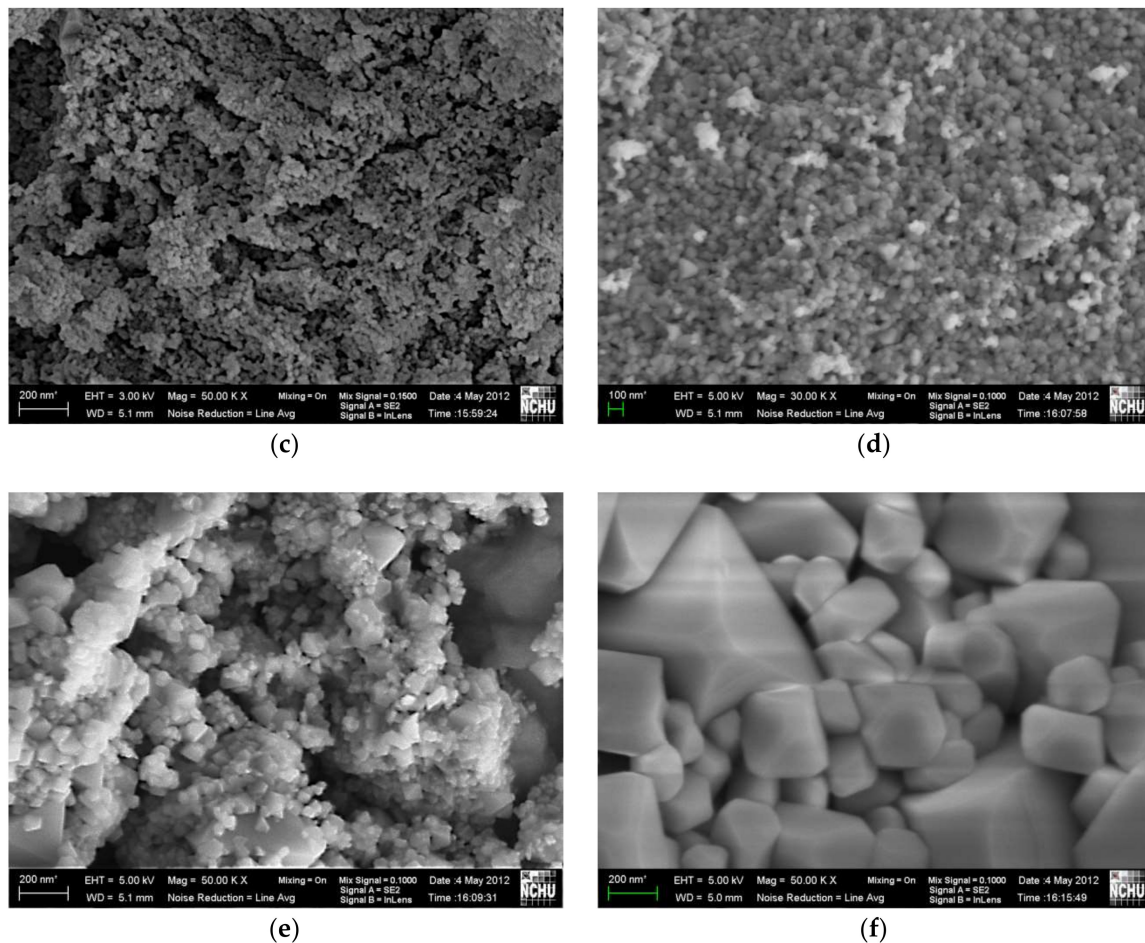
Figure 6. The surface morphologies of $Cu_{0.7}Zn_{0.3}Fe_2O_4$ at different sintering temperatures. (**a**) Not sintered (100 KX), (**b**) 500 °C, (c) 600 °C, (**d**) 700 °C, (**e**) 800 °C, (**f**) 900 °C.

3.6. Surface Morphology Analysis of $[Ni_xZn_{1-x}]Fe_2O_4$

Figure 7 shows the surface morphology of $Ni_{0.5}Zn_{0.5}Fe_2O_4$ ferrite at different sintering temperatures, under an air atmosphere at 5 °C/min, held at a constant temperature for 2 h, and then furnace-cooled. From the figure, it can be seen that the non-sintered powder had a very small particulate diameter; the average diameter was about 10 nm. When the sintering temperature increased to 500 °C, the SEM image showed that there was no significant difference, as the average particulate diameter was still about 10 nm. When the sintering temperature increased to 600 °C, the average particulate diameter increased a little, and was about 20 nm. When the sintering temperature increased to 700 °C, there was not much difference from the product sintered 600 °C, as the average particulate diameter was still about 20 nm. When the sintering temperature increased to 800 °C, the average particulate diameter became significantly larger than that sintered at 700 °C, being about 30 nm. When the sintering temperature was 900 °C, the primary particles started to cluster, and some had already associated into secondary particles, with an average particulate diameter of about 50 nm. When temperature increased to 1000 °C, the primary particles started to cluster, and a massive amount of primary particles had already associated into secondary particles, the average diameter being 60 nm. At 1100 °C, it could be seen that secondary particles crystallized in massive amounts. At 1200 °C, secondary particles started to crystallize massively, and the crystallized particles were already larger than those crystallized at 1100 °C; the crystalline surface was filled with many particles with a size of about 200 nm. $Ni_{0.5}Zn_{0.5}Fe_2O_4$ is shown in the figure with 100,000× amplification on the field emission scanning electron microscope (FESEM). After comparison of the non-sintered product (a) and

that sintered at 500 °C (b), it can be seen that the nanoparticles sintered at 500 °C were larger than the non-sintered ones by 2–3 nm. Table 3 shows the mean diameter of the $Cu_{0.7}Zn_{0.3}Fe_2O_4$ and $Ni_{0.5}Zn_{0.5}Fe_2O_4$ are correlated with the SEM and XRD size estimations according to the thermal treatments. The mean diameter of the two compositions with the same sintering temperature trend is the same. The EDS composition analysis of $Ni_{0.5}Zn_{0.5}Fe_2O_4$ showed that ferrite power was an alloy of Ni, Zn, Fe, and O. There were no other metallic ions present, and the proportion was correct, which proves that in the neutralization reaction process the metallic ions were completely precipitated.
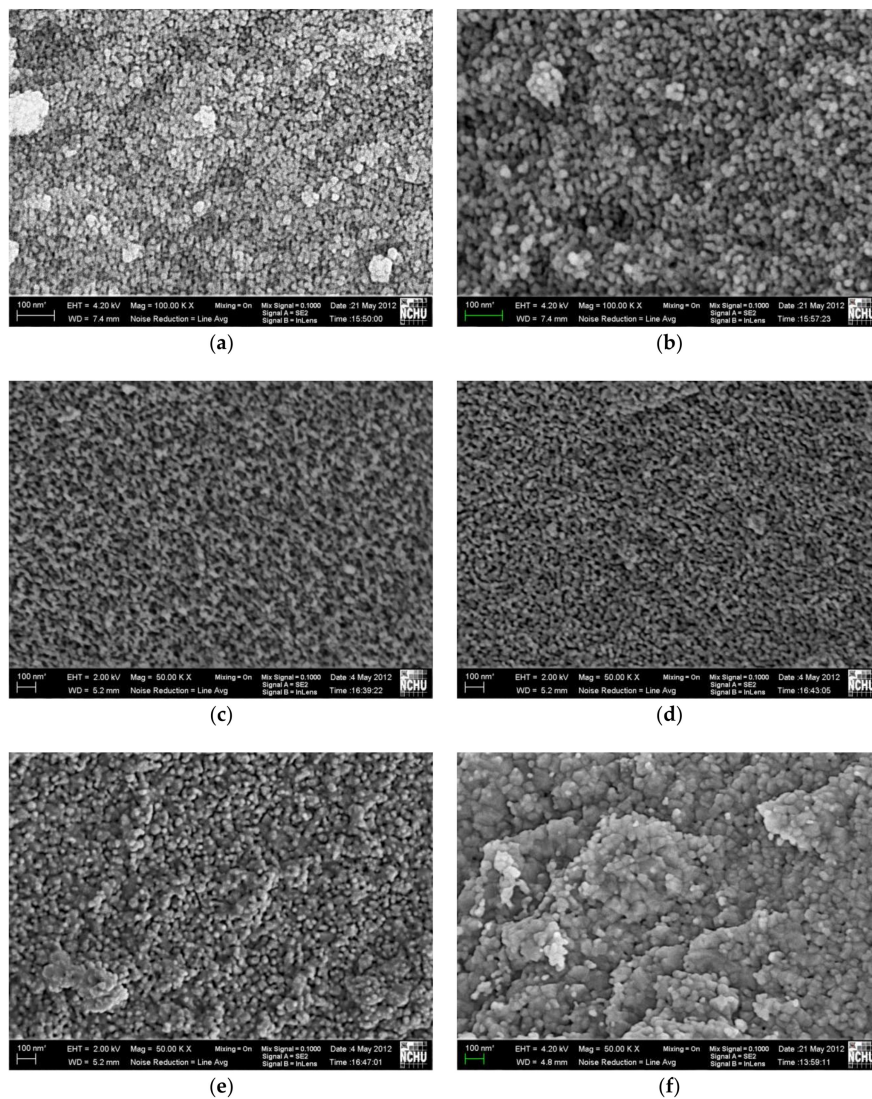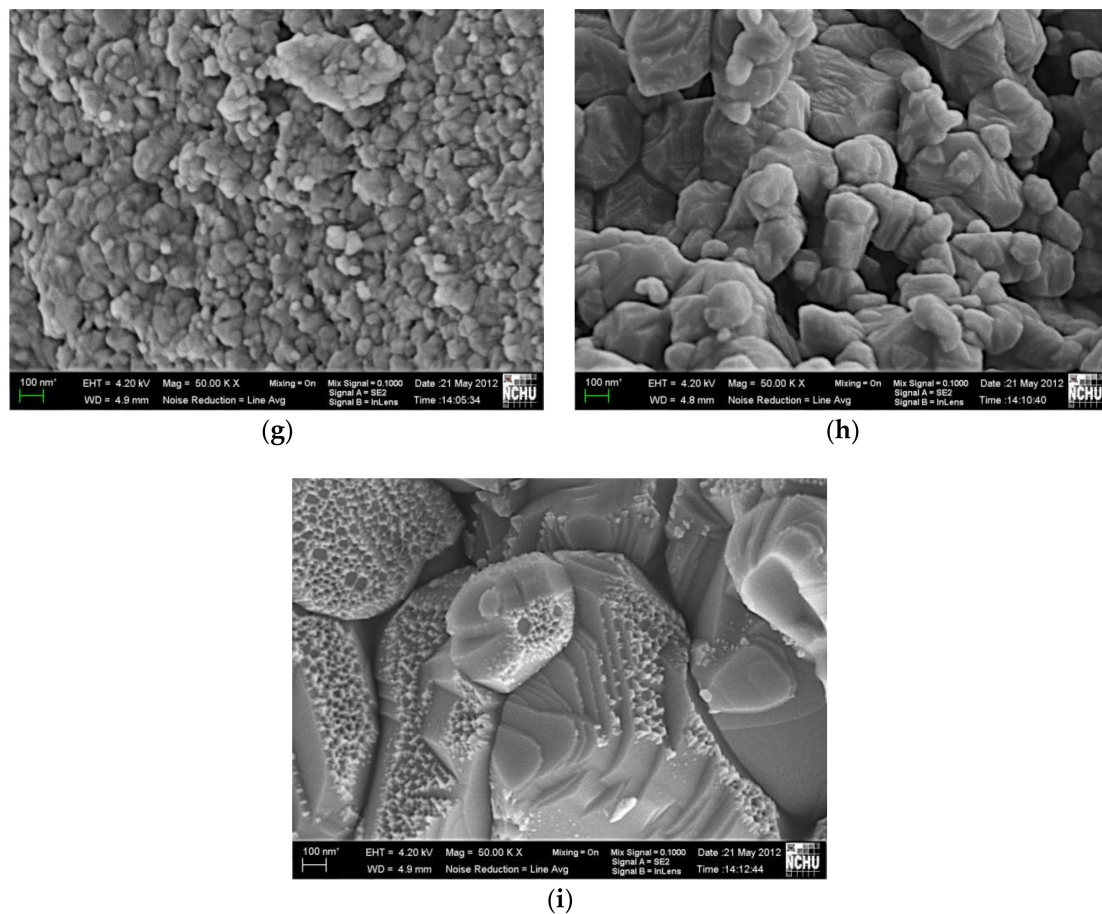

(a)

(b)

(c)

(d)

(e)

(f)

Figure 7. *Cont.*

(g)

(h)

(i)

Figure 7. The surface morphologies of $Ni_{0.5}Zn_{0.5}Fe_2O_4$ at different sintering temperatures. (**a**) Not sintered (100 KX), (**b**) 500 °C (100 KX), (**c**) 600 °C, (**d**) 700 °C, (**e**) 800 °C, (**f**) 900 °C, (**g**) 1000 °C, (**h**) 1100 °C, (**i**) 1200 °C.

**Table 3.** The effect of sintering temperature on the mean diameter.

Composition/Method Temperature,°C/ Mean Diameter	$Cu_{0.7}Zn_{0.3}Fe_2O_4$		$Ni_{0.5}Zn_{0.5}\,Fe_2O_4$	
	XRD	**SEM**	**XRD**	**SEM**
500	24.65	20	20.31	10
600	30.36	25	37.77	20
700	38.89	50	38.66	20
800	50.50	70	59.05	30
900	94.46	150	74.86	50
1000	—	—	91.86	60
1100	—	—	105.6	120
1200	—	—	201.06	250

3.7. The Influence on the Magnetic Properties of $[Ni_xZn_{1-x}]Fe_2O_4$ When Cladded with TiO_2

Figure 8 shows the hysteresis curve for $[Ni_xZn_{1-x}]Fe_2O_4$ with different proportions, cladded with TiO_2. Here, $[Ni_xZn_{1-x}]Fe_2O_4$ can be used as the carrier of the optical catalyst TiO_2, to compare its effect on the magnetic properties. From the figure, it can be seen that the material with minimal saturated magnetization was $(TiO_2)_{0.7}/Ni_{0.2}Zn_{0.8}Fe_2O_4$, which had a saturated magnetization of only 1.603 M(emu/g). As the Ni content increased, the saturated magnetization also increased, and it reached a peak for $(TiO_2)_{0.7}/Ni_{0.5}Zn_{0.5}Fe_2O_4$, which had a saturated magnetization of about 10.364 M(emu/g). This trend was the same as that for $[Ni_xZn_{1-x}]Fe_2O_4$ not cladded with TiO_2. Material magnetic measurements units (emu/g) represent magnetic susceptibility per weight.

The $(M_xZn_{1-x})Fe_2O_4$ (M=Cu, Ni) is a magnetic material, and TiO_2 is not. Therefore, the magnetic properties of the TiO_2-coated magnetic material decreased due to the dilution effect.
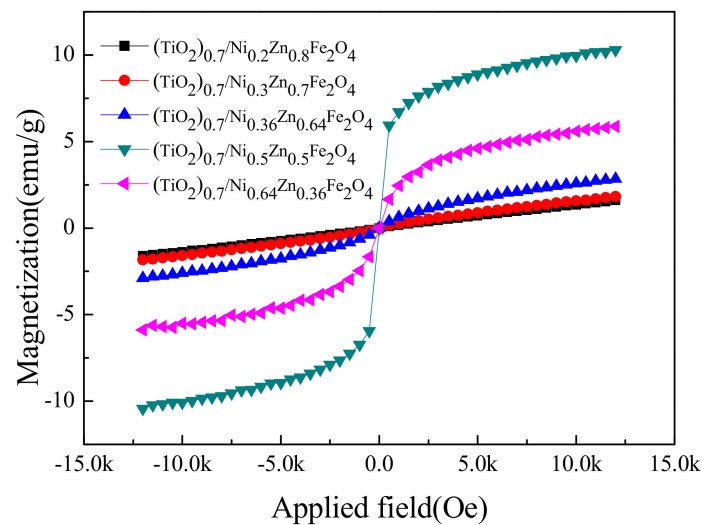
Figure 8. The influence of cladding with TiO_2 on the magnetic properties of $[Ni_xZn_{1-x}]Fe_2O_4$.

Table 4 shows the coercive force (Hc), saturated magnetization (Ms), and remanent magnetization (Mr) for $[Ni_xZn_{1-x}]Fe_2O_4$ at different proportions, cladded with TiO_2. It can be seen that, for the magnetic properties of the different systems, the Hc value did not exceed 200 Oe and the Mr value approached zero (soft ferrite had lower remanent magnetization). Therefore, all of the investigated ferrites were soft.

Table 4. The magnetic property of $[Ni_xZn_{1-x}]Fe_2O_4$ when cladded with TiO_2.

Properties of Magnetic Composition	H_C (Oe)	Ms (emu/g)	Mr (emu/g)
$(TiO_2)_{0.7}/Ni_{0.2}Zn_{0.8}Fe_2O_4$	-6.764	1.603	0.00
$(TiO_2)_{0.7}/Ni_{0.3}Zn_{0.7}Fe_2O_4$	15.677	2.865	0.01
$(TiO_2)_{0.7}/Ni_{0.36}Zn_{0.64}Fe_2O_4$	12.195	1.832	0.00
$(TiO_2)_{0.7}/Ni_{0.5}Zn_{0.5}Fe_2O_4$	9.912	10.364	-0.04
$(TiO_2)_{0.7}/Ni_{0.64}Zn_{0.36}Fe_2O_4$	-3.391	5.877	-0.01

4. Conclusions

After summarizing the experimental results obtained from $[Cu_xZn_{1-x}]Fe_2O_4$ and $[Ni_xZn_{1-x}]Fe_2O_4$, the following conclusions can be obtained: for different compositions of Cu-Zn and Ni-Zn ferrites, the sintering temperatures for optimal saturated magnetization values were quite different. For the $[Cu_xZn_{1-x}]Fe_2O_4$ system, the optimal sintering temperature was 900 °C, and the saturated magnetization was 60.19 M(emu/g). For the $[Ni_xZn_{1-x}]Fe_2O_4$ system, the optimal sintering temperature was also 900 °C, but the saturated magnetization was 91.40 M(emu/g). The material with the saturated magnetization most seriously affected by the sintering temperature was $[Ni_xZn_{1-x}]Fe_2O_4$, and the difference between the maximal and minimal values was 41.11 M(emu/g). However, for the $[Cu_xZn_{1-x}]Fe_2O_4$ system, the difference between the maximal and minimal value was 35.30 M(emu/g). The size of the remanent magnetization depended on the preparation conditions, and there was no relative relationship between the size of the saturated magnetization and the size of the remanent magnetization. Moreover, there was no relative relationship between the size of the saturated magnetization and the size of the coercive force. Both for Cu-Zn and Ni-Zn ferrites, the coercive force did not exceed 200 Oe; thus, both materials were

soft ferrites. From VSM and XRD results for the different compositions, it can be seen that, for all kinds of systems and all proportions, the sintering atmosphere and sintering temperature—before the drop of the saturated magnetization—indicated that the stronger the crystal phase strength, the stronger the saturated magnetization. For $[Cu_xZn_{1-x}]Fe_2O_4$ and $[Ni_xZn_{1-x}]Fe_2O_4$ ferrites at different sintering temperatures, the crystal phase strength of XRD was affected; the higher the sintering temperature, the stronger the crystal phase. For the material with a stronger crystal phase, SEM showed that the average particulate diameter was also larger, and when the sintering temperature was higher, the average particulate diameter was larger. It can be clearly seen from the SEM photos that, for non-sintered to sintered at 900 °C Cu-Zn and Ni-Zn ferrites, the one with the maximal change on the average particulate diameter due to sintering temperature was $[Cu_xZn_{1-x}]Fe_2O_4$, and the average particulate diameter changed from 10 nm to 150 nm; for the $[Ni_xZn_{1-x}]Fe_2O_4$ system, the average particulate diameter change was in the range of 10–50 nm.

Author Contributions: Yenchun Liu conceived and designed the experiments; Yenchun Liu and Jarnchih Hsu performed the experiments; Yenchun Liu and Jarnchih Hsu analyzed the data; Yenchun Liu contributed reagents/materials/analysis tools; Yenchun Liu wrote the paper.

Conflicts of Interest: The authors declare no conflict of interest. The founding sponsors had no role in the design of the study; in the collection, analyses, or interpretation of data; in the writing of the manuscript, and in the decision to publish the results.

References

1. Smit, J.; Wijn, H.P.J. *Ferrites*; Philips Technical Library: Eindhoven, The Netherlands, 1959.
2. Murdock, E.S.; Simmons, R.F.; Davidson, R. Roadmap for 10 Gbit/in2 Media: Challenges. *IEEE Trans. Magn.* **1992**, *28*, 3078–3083. [CrossRef]
3. Standley, K.J. *Oxide Magnetic Materials*, 2nd ed.; Oxford University Press: Oxford, UK, 1972.
4. Emad, M.M.E.; Mahmoud, M.M.; Abdel-Hady, E.A. In-Situ synthesis of Magnetic Mn-Zn Ferrite ceramic object by solid state reaction. *J. Aust. Ceram. Soc.* **2008**, *44*, 57–62.
5. Zheng, Z.G.; Zhong, X.C.; Zhang, Y.H.; Yu, H.Y. Synthesis structure and magnetic properties of nanocrystalline $Zn_xMn_{1-x}Fe_2O_4$ prepared by ball milling. *J. Alloys Comp.* **2008**, *466*, 377–382. [CrossRef]
6. Ammad, Q.H. The influence of hafnia and impurities (CaO/SiO_2) on the microstructure and magnetic properties of Mn-Zn ferrites. *J. Cryst. Growth* **2006**, *286*, 365–370.
7. Upadhyay, C.; Verma, H.C.; Rath, C.; Sahu, K.K.; Anand, S.; Das, R.P.; Mishra, N.C. Mossbauer studies of nanosize $Mn_{1-x}Zn_xFe_2O_4$. *J. Alloys Comp.* **2001**, *326*, 94–97. [CrossRef]
8. Arulmurugan, R.; Vaidyanathan, G.; Sendhilnathan, S.; Jeyadevan, B. Mn-Zn ferrite nanoparticles for ferrofluid preparation: Study on thermal-magnetic properties. *J. Magn. Magn. Mater.* **2006**, *298*, 83–94. [CrossRef]
9. Peng, X.; Peng, K.; Huang, J. Synthesis and magnetic properties of core-shell structured Finemet/Ni-Zn ferrite soft nanocomposites by co-precipitation. *J. Alloys Comp.* **2017**, *691*, 165–170. [CrossRef]
10. Mane, D.R.; Patil, S.; Birajdar, D.D.; Kadam, A.B.; Shirsath, S.E.; Kadam, R.H. Sol-gel synthesis of Cr^{3+} substituted $Li_{0.5}Fe_{2.5}O_4$:cation distribution, structural and magnetic properties. *J. Mater. Chem. Phys.* **2011**, *126*, 755–760. [CrossRef]
11. Song, F.; Shen, X.; Liu, M.; Xiang, J. Preparation and magnetic properties of $SrFe_{12}O_{19}/Ni_{0.5}Zn_{0.5}Fe_2O_4$ nanocomposite ferrite microfibers via sol-gel process. *J. Mater. Chem. Phys.* **2011**, *126*, 791–796. [CrossRef]
12. Ghoul, E.; Kraini, M.; Lemine, O.M.; Mir, L.E. Sol–gel synthesis, structural, optical and magnetic properties of Co-doped ZnO nanoparticles. *J. Mater. Sci. Mater. Electron.* **2015**, *26*, 2614–2621. [CrossRef]
13. Pozo, G.L.; Silvetti, S.P.; Aguirre, M.C.; Condo, A.M. Synthesis and characterization of $(NiZnFe_2O_4)_{0.5}/(SiO_2)_{0.5}$ granular nanocomposites. *J. Alloys Comp.* **2009**, *487*, 646–652. [CrossRef]
14. Lu, X.; Zhou, T.; Jia, M. Hydrothermal synthesis of Mn-Zn ferrites from spent alkaline Zn-Mn batteries. *J. Particuol.* **2009**, *7*, 491–495.

15. Nejati, K.; Zabihi, R. Preparation and magnetic properties of nano size nickel ferrite particles using hydrothermal method. *Chem. Cent. J.* **2012**, *6*, 23–29. [CrossRef] [PubMed]

16. Reddy, L.H.; Arias, J.L.; Nicolas, J.; Couvreur, P. Magnetic Nanoparticles: Design and Characterization, Toxicity and Biocompatibility, Pharmaceutical and Biomedical Applications. *Chem. Rev.* **2012**, *112*, 5818–5878. [CrossRef] [PubMed]

17. Liu, X.; Cheng, B.; Hu, J.; Qin, H.; Jiang, M. Semiconducting gas sensor for ethanol based on $LaMg_xFe_{1-x}O_3$ nanocrystal. *Sens. Actuat. B* **2008**, *129*, 53–58. [CrossRef]

18. Hsu, W.C.; Chen, S.C.; Kuo, P.C.; Lie, C.T.; Tsai, W.S. Preparation of NiCuZn ferrite nanoparticles from chemical co-precipitation method and the magnetic properties after sintering. *J. Mater. Sci. Eng. B* **2004**, *111*, 142–149. [CrossRef]

19. Gabal, M.A.; Abdel-Daiem, A.M.; Angari, Y.M.; Ismail, I.M. Influence of Al-substitution on structural, electrical and magnetic properties of Mn–Zn ferrites nanopowders prepared via the sol–gel auto-combustion method. *Polyhedron* **2013**, *57*, 105–111. [CrossRef]

20. Mürbe, J.; Töpfer, J. Ni-Cu-Zn Ferrites for Low Temperature Firing: I. Ferrite Composition and its effect on sintering behavior and permeability. *J. Electr.* **2005**, *15*, 215–221. [CrossRef]

21. Meiklejohn, W.H.; Bean, C.P. New magnetic anisotropy. *Phys. Rev. J. Arch.* **1956**, *102*, 1413. [CrossRef]

22. Kumar, A.; Annveer; Arora, M.; Yadav, M.S.; Panta, R.P. Induced size effect on Ni doped Nickel Zinc Ferrite Nanoparticles. *Phys. Proc.* **2010**, *9*, 20–23. [CrossRef]

23. Zhu, X.R.; Zhu, Z.G.; Chen, C.; Shen, F.L. Structural, Infrared and Magnetic Properties of Nanosized $Ni_xZn_{1-x}Fe_2O_4$ Powders Synthesized by Sol–Gel Technique. *J. Nanosci. Nanotechnol.* **2015**, *15*, 3182–3186. [CrossRef] [PubMed]